Draft version June 26, 2020
Typeset using LaTeX **twocolumn** style in AASTeX62

Perseus ALMA Chemistry Survey (PEACHES). I. The Complex Organic Molecules of Embedded Protostars

Yao-Lun Yang,[1,2] Nami Sakai,[2] and Yichen Zhang[2]

[1] *Department of Astronomy, University of Virginia, Charlottesvile, VA 22904-4235, USA*
[2] *RIKEN Cluster for Pioneering Research, Wako-shi, Saitama, 351-0106, Japan*

1. INTRODUCTION

Planet formation may start during the embedded phase of star formation. In the scenario where planets form from the embedded disks, resulting in substructures, the chemistry of embedded disks may play a significant role for the chemical composition of the forming planets. In the recent years, observations discover the emission of unsaturated complex organic molecules such as carbon-chain molecules (e.g., Sakai & Yamamoto 2013; Sakai et al. 2014; Law et al. 2018) and the saturated complex organic molecules (COMs, Cazaux et al. e.g., 2003; Bottinelli et al. e.g., 2007; Jorgensen et al. e.g., 2020) toward the center of several protostellar cores, indicating that embedded protostars have developed a complex chemistry at the disk-forming region. The saturated organic molecules have single covalent bonds for all atoms, making them rich in hydrogen, while the unsaturated organic molecules contain double or triple bonds between carbon atoms, making them poor in hydrogen. If the forming planets inherit the chemistry of embedded disks, the abundance of complex organic molecules may implicate future developments of organics on the planets.

Heavier or more complex molecules, such as cyclic-C_3H_2, SO, and complex organic molecules (COMs), are in the gas phase at the inner protostellar envelope ($T \gtrsim 100$ K), which coincidentally corresponds to ~ 100 au for typical low-mass protostars (Yang et al. 2020). Thus, COMs exclusively trace the properties of the inner envelope where a disk may be forming (Aikawa 2013; Sakai et al. 2014). The kinematics of a rotating infalling envelope has been analyzed with the observations of heavier or more complex molecules, such as CH_3OH and CH_2DOH for HH 212 (Lee et al. 2017), CS for IRAS 04365+2535 (Sakai et al. 2016) and L483 (Oya et al. 2017), cyclic-C_3H_2 for L1527 (Sakai et al. 2014), OCS for IRAS 16293−2422 A (Oya et al. 2016), and methanol and HCOOH for B335 (Imai et al. 2019).

Corresponding author: Yao-Lun Yang
yaolunyang.astro@gmail.com

While recent observations show several embedded protostars with rich spectra of complex molecules, the occurrence of complex molecules at embedded protostars and its relationship to the star formation process remain poorly understood. Several protostars are rich in COMs but show little emission of long carbon-chain molecules, such as IRAS 16293−2422 (Jørgensen et al. 2016), NGC 1333 IRAS 4A (Bottinelli et al. 2004; Sahu et al. 2019), and B335 (Imai et al. 2016, 2019); some protostars are rich in long carbon-chain molecules but not in COMs, such as L1527 (Sakai et al. 2010) and IRAS 15398−3359 (Sakai et al. 2009). While the bimodal chemical appearance hints a bimodal evolutionary path, the chemical pathways of complex molecules at the embedded protostars remain ill-constrained as a few protostars show the emission of both COMs and long carbon-chain molecules at different scales, such as L483 (Oya et al. 2017). Recent surveys show lack of correlations between COMs and long carbon-chain molecules, suggesting that observational biases may contribute to the apparent bimodal chemistry (Graninger et al. 2016; Higuchi et al. 2018) (reference).

Perseus molecular cloud is one of the most active nearby star-forming region, which extends ∼10 pc on the sky. Infrared and submillimeter surveys reveal more than 400 young stellar objects as well as ∼100 dense cores, which contains ∼50 Class 0 and I protostars (Hatchell et al. 2005; Jørgensen et al. 2008; Dunham et al. 2013; hereafter the embedded protostars). The Perseus molecular cloud contains star-forming regions in a wide range of environments. The majority of protostars in Perseus are associated with two clusters, NGC 1333 and IC 348. NGC 1333 has significant outflow activity (reference) and a younger age than that of IC 348. The embedded protostars associated with IC 348 lie at the southwest of IC 348 near a prominent outflow, HH 211 (reference). Most of other embedded protostars at Perseus are related to L1448, L1455, Bernard 1 (B1), and Bernard 5 (B5). L1448 has active outflows that may regulate the ongoing star formation (Curtis et al. 2010); The protostars in L1455 are slightly more evolved than that in other regions; (reference) B1 exhibits rich spec-

tra of deuterated species (reference). Thus, the Perseus molecular cloud provides the ideal test bed for chemistry in embedded protostars by surveying the protostars within each region and across the entire cloud.

Higuchi et al. (2018) presented a pilot survey of the chemistry in the Perseus embedded protostars with Nobeyama 45m telescope, which survey all Class 0/I protostars (Hatchell et al. 2007) that have the bolometric luminosity ($L_{\rm bol}$) greater than 1 $L_\odot$ (0.7 $L_\odot$for protostars in B1 and B5) and the envelope mass greater than 1 $M_\odot$. This pilot survey probes the molecules such as C_2H, c-C_3H_2, and CH_3OH and find the majority of the sources are neither only rich in CH_3OH or carbon-chain molecules. They also suggest a possible correlation between the location of sources within the clouds and the chemistry. Other surveys with single-dish telescopes also characterize the COMs abundance at embedded protostars and test the chemical models (e.g., Bergner et al. 2017). Due to the large beam, chemistry survey with single-dish telescopes often more sensitive to COMs in cool temperature (10–20 K), which may not be directly associated with the COMs thermally desorbed from icy grains. Interferometry is crucial for probing the warm COMs at embedded protostars. With 26 embedded protostars from several star-forming regions, Belloche et al. (2020) find CH_3OH in about half fo the sample as well as other more complex COMs. They also investigate the potential origin of COMs and reveal apparent chemical difference among multiple systems. Despite of the growing sample of COMs detections in embedded protostars, the statistics of COMs occurrence and abundance remain unconstrained due to the biases from the source selection and the limited resolution. To unbiasedly survey the chemistry, we conducted the Perseus ALMA Chemistry Survey (PEACHES) that probes the complex chemistry toward Perseuse embedded protostars. The source selection follows the same criteria as Higuchi et al. (2018) with a few pointing modifications using the results from the VLA Nascent Disk and Multiplicity Survey (VANDAM) of Perseus protostars (Tobin et al. 2016).

Section 2 describes the details of our ALMA observations. Section XXX

2. OBSERVATIONS

The PEACHES observations were conducted in two ALMA projects (2016.1.01501.S and 2017.1.01462.S; PI: N. Sakai), surveying 37 fields toward the Perseus molecular cloud. Table 1 lists the details about the ALMA projects used in this study. ALMA correlator was configured to have 13 spectral windows (spw) at Band 6, which have 12 narrow spws with 480 channels and a wide spw with 980 channels. The narrow spws were tuned to observe specific molecular species, such as SiO, CS, CH_3OH and CH_3CN, with a spectral resolution of 122 kHz ($\sim$0.15 km s^{-1}), while the wide spw aimed to observe the continuum with a resolution of 0.976 MHz ($\sim$0.4 km s^{-1}). The frequency setup for the two ALMA projects are largely identical except for the wide continuum window (spw04), which shifts by $\sim$620 MHz. Table 2 lists the frequency ranges for each spw.

We use CASA (McMullin et al. 2007) for standard calibration and imaging of the continuum and spectral lines with `tclean`. Because of the rich spectra, we manually flag the lines for the continuum imaging. The spectra of spw10 and spw11 are combined for the imaging because the broad SiO emission. The spectra is cleaned down to 0.022 Jy, except for the spw04, which is cleaned down to 0.008 Jy due to its lower spectral resolution. The line imaging used the "multiscale" deconvolver with a robust parameter of 0.5, because the targeted emission traces different spatial scales (e.g. SiO for outflows and COMs for the inner envelope/disk).

The synthesized beam is about $0\farcs6\times0\farcs4$ (Table 3). The Perseus molecular cloud is not at a single distance. Many studies assume a distance of 235 pc for Perseus based on the maser observations toward NGC 1333 SVS 13 (Hirota et al. 2008). Recently, Ortiz-León et al. (2018) derive a distance of 321$\pm$10 pc for IC 348 using VLBA and a distance of 293$\pm$22 pc for NGC 1333 using *Gaia* parallaxes. Zucker et al. (2020) combine the *Gaia* parallaxes and photometric data with a Bayesian framework to revise the distances toward different sightlines of Perseus, resulting in distances ranging from 234 pc to 331 pc. In this study, we assume a distance of 300 pc for the entire Perseus cloud. Thus, the synthesized beam is about 180 au$\times$120 au.

3. ANALYSES

3.1. *Identification of Young Stellar Object*

In the 37 field of view, 51 continuum peaks are identified. We use the CASA task `imfit` to iteratively fit for continuum sources down to 5σ of the residual image within the central 70% of the primary beam size (20″). For the field centered on Per-emb 16, the fitting uses a threshold of 4σ and extends the mask to the entire primary beam as a continuum source, Per-emb 28, is detected toward the edge of the primary beam where the noise is elevated. The continuum of the multiple systems are manually fitted to the individual continuum peak. Two protostars, L1448 IRS 2E and SVS 3, become non-detection in our observations due to their low brightness. SVS 13C locates at the edge of the primary beam, resulting in a noisy continuum. Thus, we exclude

Table 1. ALMA Projects for PEACHES

Project code	Observation time	Amplitude calibrator	Bandpass calibrator	Phase calibrator
2016.1.01501.S	2016-11-16, 19, 26, 29, 30	J0238+1636	J0237+2848	J0336+3218
2017.1.01462.S	2018-09-10, 12	J0237+2848	J0237+2848	J0336+3218

Table 2. Frequency Setup

Spectral window	2016.1.01501.S		2017.1.01462.S	
	frequemcy range	channel width	frequency range	channel width
spw00	243.483–243.542 GHz	122.070 kHz	243.502–243.561 GHz	122.070 kHz
spw01	243.878–243.937 GHz	122.070 kHz	243.897–243.956 GHz	122.070 kHz
spw02	244.200–244.259 GHz	122.070 kHz	244.219–244.278 GHz	122.070 kHz
spw03	244.898–244.957 GHz	122.070 kHz	244.917–244.975 GHz	122.070 kHz
spw04	246.186–247.124 GHz	976.562 kHz	245.805–246.743 GHz	976.562 kHz
spw05	257.489–257.548 GHz	122.070 kHz	257.509–257.568 GHz	122.070 kHz
spw06	258.218–258.276 GHz	122.070 kHz	258.238–258.296 GHz	122.070 kHz
spw07	259.288–259.347 GHz	122.070 kHz	259.308–259.366 GHz	122.070 kHz
spw08	258.974–259.032 GHz	122.070 kHz	258.993–259.052 GHz	122.070 kHz
spw09	262.046–262.104 GHz	122.070 kHz	262.066–262.124 GHz	122.070 kHz
spw10_spw11[a]	260.442–260.551 GHz	122.070 kHz	260.462–260.571 GHz	122.070 kHz
spw12	261.787–261.845 GHz	122.070 kHz	261.807–261.865 GHz	122.070 kHz

[a] The spectra of spw10 and spw11 are combined to measure the baseline due to the broad SiO emission.

SVS 13C from this study, making a total of 50 protostars. L1448 IRS 2E has CS emission.

Figure 1 shows the continuum emission along with the fitted shapes, while Table 3 lists the properties of the continuum sources. The continuum emission peak appears as a compact circular or elliptical shape. Some sources show extended continuum emission resembling the shape of outflow cavities, such as Per-emb 22 A and B. Three sources, EDJ2009-237, Per-emb 60, and EDJ2009-172, show no spectral line and no reliable measurement of source velocity in literature; therefore, we exclude them from spectral extraction as well as the line identification and modeling. However, these three sources still contribute to the total number of sources for calculating the detection statistics.

The observations resolve or marginally resolve 90% (45 of 50) of the continuum sources. Our sample includes single sources as well as resolved and unresolved multiple systems. According to the VANDAM survey (Tobin et al. 2016), our sample contains eleven binary systems and one triple system. Two of eleven binary systems are resolved and the triple system appears as a single source and an unresolved binary. In total, 20% of the sources are unresolved binary.

Tychoniec et al. (2020) derive the central dust mass of Perseus protostars using the 9 mm VLA observations (VANDAM; see Table 3). Dust emission from the center of a protostar may be marginally optically thick at millimeter wavelengths (Ko et al. 2020), making the derived dust mass lower limits. Seven sources in our sample have the averaged continuum brightness temperature exceeding 10 K (Table 3). NGC 1333 IRAS 4A1 has a T_b of 21.9 K, the brightest among our sample. In fact, continuum opacity limits the detectability of COMs toward 4A1, where COMs appear as absorption at ALMA Band 7 (Sahu et al. 2019) and emission at centimeter wavelengths (De Simone et al. 2020). Toward the other six sources, Per-emb 33 A, NGC 1333 IRAS 4A2, NGC 1333 IRAS 4B1, Per-emb 5, B1-b S, and Per-emb 11 A, our observations detect several molecular lines from the central region, suggesting that the continuum opacity has less impact compared to that for IRAS 4A1. Previous observations also suggest less impact from the continuum opacity for NGC 1333 IRAS 4B1 (Belloche et al. 2020) and B1-b S (Marcelino et al. 2018). Most of the sources show averaged brightness temperatures lower than 10 K, suggesting that the continuum sources remain unresolved and have a negligible effect to the COMs emission. We take the T_b as a tracer of the averaged dust column densities. Constraining the actual column densities requires higher resolution observations.

Table 3. PEACHES Sample

Source	Common names	R.A. (J2000)	Decl. (J2000)	$v_{\rm lsr}$	Ref. ($v_{\rm lsr}$)	Beam	Cont. Size	$T_{\rm cont}$	$M_{\rm dust}$ [a]
		(hh:mm:ss)	(dd:mm:ss)	(km s^{-1})		($''$)	($''$)	(K)	($M_\oplus$)
Per-emb 22 B		03:25:22.35	30:45:13.11	4.3	S19	$0.''64\times0.''39$	$0.''95\times0.''51$	0.92	23.1±13.0
Per-emb 22 A		03:25:22.41	30:45:13.26	4.3	S19	$0.''64\times0.''39$	$0.''86\times0.''65$	1.71	96.4±24.1
L1448 NW	L1448 IRS 3C	03:25:35.67	30:45:34.16	4.2	H18	$0.''64\times0.''39$	$0.''83\times0.''47$	3.15	382.4±54.9
Per-emb 33 B/C		03:25:36.32	30:45:15.19	5.3	S19	$0.''64\times0.''39$	$0.''75\times0.''48$	5.55	226.4±43.7
Per-emb 33 A		03:25:36.38	30:45:14.72	5.3	S19	$0.''64\times0.''39$	$0.''73\times0.''45$	10.33	294.0±57.6
L1448 IRS 3A		03:25:36.50	30:45:21.90	4.6	H18	$0.''64\times0.''39$	$0.''85\times0.''59$	3.21	235.1±47.8
Per-emb 26		03:25:38.88	30:44:05.28	5.4	S19	$0.''64\times0.''39$	$0.''69\times0.''45$	8.03	636.1±102.5
Per-emb 42		03:25:39.14	30:43:57.90	5.8	S19	$0.''64\times0.''39$	$0.''64\times0.''39$	0.66	116.5±29.0
Per-emb 25	IRAS 03235+3004	03:26:37.51	30:15:27.81	5.5	S18	$0.''64\times0.''39$	$0.''69\times0.''41$	5.27	172.6±65.4
Per-emb 17	L1455 IRS 1, IRAS 03245+3002	03:27:39.11	30:13:02.96	6.0	S19	$0.''64\times0.''40$	$0.''79\times0.''48$	2.00	199.4±34.0
Per-emb 20	L1455 IRS 4	03:27:43.28	30:12:28.88	5.3	S19	$0.''64\times0.''40$	$1.''29\times0.''78$	0.14	<31.1±15.5
L1455 IRS 2		03:27:47.69	30:12:04.33	5.1	H18	$0.''64\times0.''40$	$0.''60\times0.''38$	0.13	23.3±13.3
Per-emb 35 A	NGC 1333 IRAS 1	03:28:37.10	31:13:30.77	7.4	Y20	$0.''66\times0.''42$	$0.''75\times0.''51$	0.93	47.0±15.7
Per-emb 35 B	NGC 1333 IRAS 1	03:28:37.22	31:13:31.74	7.3	Y20	$0.''66\times0.''42$	$0.''78\times0.''53$	0.75	86.8±20.6
Per-emb 27	NGC 1333 IRAS 2A	03:28:55.57	31:14:36.97	6.5	Y20	$0.''66\times0.''42$	$0.''93\times0.''66$	5.79	683.7±93.6
EDJ2009-172		03:28:56.65	31:18:35.43	···	···	$0.''66\times0.''42$	$0.''69\times0.''44$	0.62	196.4±20.0
Per-emb 36	NGC 1333 IRAS 2B	03:28:57.37	31:14:15.77	6.9	S19	$0.''66\times0.''42$	$0.''73\times0.''46$	5.56	666.5±93.4
Per-emb 54	NGC 1333 IRAS 6	03:29:01.55	31:20:20.49	7.9	S19	$0.''66\times0.''42$	$0.''69\times0.''40$	0.07	115.5±28.2
SVS 13B	NGC 1333 SVS 13B	03:29:03.08	31:15:51.73	8.5	S19	$0.''66\times0.''42$	$0.''87\times0.''68$	6.64	581.1±98.2
SVS 13A2	VLA 3	03:29:03.39	31:16:01.58	8.4	S18	$0.''66\times0.''42$	$0.''86\times0.''53$	0.61	102.6±27.7
Per-emb 44	NGC 1333 SVS 13A	03:29:03.76	31:16:03.70	8.7	S19	$0.''66\times0.''42$	$0.''98\times0.''79$	6.84	674.4±90.9
Per-emb 15		03:29:04.06	31:14:46.23	6.8	S19	$0.''66\times0.''42$	$0.''89\times0.''70$	0.17	<9.3±6.6
Per-emb 50	IRAS 03260+3111 A	03:29:07.77	31:21:57.11	9.3	Y20	$0.''66\times0.''42$	$0.''73\times0.''44$	4.13	535.2±91.0
Per-emb 12 B	NGC 1333 IRAS 4A2	03:29:10.44	31:13:32.08	6.9	S19	$0.''66\times0.''42$	$1.''33\times0.''81$	10.04	158.1±38.4
Per-emb 12 A	NGC 1333 IRAS 4A1	03:29:10.54	31:13:30.93	6.9	S19	$0.''66\times0.''42$	$1.''11\times0.''98$	21.85	2853.9±437.0
Per-emb 21	NGC 1333 IRAS 7 SM2	03:29:10.67	31:18:20.16	8.6	Y20	$0.''66\times0.''42$	$0.''74\times0.''48$	2.05	211.9±41.1
Per-emb 18	NGC 1333 IRAS 7 SM1	03:29:11.27	31:18:31.09	8.1	S19	$0.''66\times0.''42$	$0.''84\times0.''73$	3.42	224.8±47.1
Per-emb 13	NGC 1333 IRAS 4B1	03:29:12.02	31:13:07.99	7.1	S19	$0.''66\times0.''42$	$1.''07\times0.''83$	14.76	1271.3±207.6
IRAS4B'	NGC 1333 IRAS 4B2	03:29:12.85	31:13:06.87	7.1	S19	$0.''66\times0.''42$	$0.''83\times0.''74$	7.13	603.2±115.2
Per-emb 14	NGC 1333 IRAS 4C	03:29:13.55	31:13:58.12	7.9	S19	$0.''66\times0.''42$	$0.''79\times0.''50$	3.05	311.2±58.6
EDJ2009-235		03:29:18.26	31:23:19.73	7.7	Y20	$0.''67\times0.''42$	$0.''66\times0.''44$	0.26	16.6±10.0
EDJ2009-237		03:29:18.74	31:23:25.24	···	···	$0.''67\times0.''42$	$0.''67\times0.''42$	0.12	···
Per-emb 37		03:29:18.97	31:23:14.28	7.5	Y20	$0.''67\times0.''42$	$0.''82\times0.''57$	0.56	95.4±23.9
Per-emb 60		03:29:20.05	31:24:07.35	···	···	$0.''67\times0.''42$	$0.''73\times0.''47$	0.08	<13.3±8.1
Per-emb 5	IRAS 03282+3035	03:31:20.94	30:45:30.24	7.3	S19	$0.''45\times0.''30$	$0.''56\times0.''41$	15.29	502.3±86.3
Per-emb 2	IRAS 03292+3039	03:32:17.92	30:49:47.81	7.0	S19	$0.''45\times0.''30$	$1.''35\times0.''97$	7.41	927.4±175.6
Per-emb 10	B1-d	03:33:16.43	31:06:52.01	6.4	S19	$0.''46\times0.''30$	$0.''49\times0.''32$	1.82	143.4±30.7
Per-emb 40	B1-a	03:33:16.67	31:07:54.87	7.4	S19	$0.''46\times0.''30$	$0.''47\times0.''32$	1.44	72.9±18.0
Per-emb 29	B1-c	03:33:17.88	31:09:31.74	6.1	Y20	$0.''46\times0.''30$	$0.''56\times0.''39$	8.41	233.5±43.5
B1-b N		03:33:21.21	31:07:43.63	6.6	C16	$0.''46\times0.''30$	$0.''56\times0.''47$	7.67	483.8±85.1
B1-b S		03:33:21.36	31:07:26.34	6.6	C16	$0.''46\times0.''30$	$0.''63\times0.''53$	14.79	354.0±76.5
Per-emb 16		03:43:50.97	32:03:24.12	8.8	S19	$0.''50\times0.''32$	$0.''61\times0.''52$	0.35	<34.9±18.1
Per-emb 28		03:43:51.01	32:03:08.02	8.6	S19	$0.''50\times0.''32$	$0.''56\times0.''32$	1.52	23.5±16.6
Per-emb 1	HH 211 MMS	03:43:56.81	32:00:50.16	9.4	S19	$0.''49\times0.''32$	$0.''68\times0.''48$	4.57	279.6±50.0
Per-emb 11 B	IC 348 MMS	03:43:56.88	32:03:03.08	9.0	S19	$0.''50\times0.''33$	$0.''92\times0.''69$	0.40	21.7±14.9
Per-emb 11 A	IC 348 MMS	03:43:57.07	32:03:04.76	9.0	S19	$0.''50\times0.''33$	$0.''61\times0.''48$	10.47	413.5±73.1
Per-emb 11 C	IC 348 MMS	03:43:57.70	32:03:09.82	9.0	S19	$0.''50\times0.''33$	$1.''10\times0.''86$	0.34	30.5±15.4
Per-emb 55	IRAS 03415+3152	03:44:43.30	32:01:31.22	12.0	S19	$0.''50\times0.''32$	$0.''49\times0.''33$	0.32	56.1±12.9
Per-emb 8		03:44:43.98	32:01:35.19	11.0	S19	$0.''50\times0.''32$	$0.''49\times0.''36$	8.51	237.9±47.5
Per-emb 53	B5 IRS 1	03:47:41.59	32:51:43.62	10.2	Y20	$0.''51\times0.''33$	$0.''58\times0.''42$	1.55	56.6±22.6

References—C16=Carney et al. (2016); H18=Higuchi et al. (2018); S18=Stephens et al. (2018); S19=Stephens et al. (2019); Y20=this study.

[a] The dust mass is taken from Tychoniec et al. (2020).

NOTE—The dust masses for L1455 IRS 2, EDJ2009-235, EDJ2009-172 are taken from Tychoniec et al. (2018) by applying a gas-to-dust ratio of 100. The dust mass of unresolved multiple systems, such as L1448 NW, Per-emb 33 B/C, Per-emb 17, Per-emb 44, Per-emb 27, Per-emb 36, and Per-emb 55, are taken to be the total mass of multiple protostars. The dust mass of Per-emb 40 is assumed to be the dust mass of Per-emb 40 A as the dust mass of Per-emb 40 B is an upper limit.

3.2. *Spectral Extraction*

The ALMA image cubes are post-processed to extract 1D spectra for identifying the emission of complex molecules and further analyses. COMs typically desorb from dust grains at $T \gtrsim 100$ K, which coincidentally corresponds to $\sim$ 100 au for typical embedded protostars (e.g., Yang et al. 2020). Given the spatial resolution of $\sim$0.″5 ($\sim$150 au), we focus on the spectra toward the continuum sources to search for the COMs in the inner envelope. In most of the cases, COMs emission concentrates around the protostars at $\lesssim$300 au scale. Figure 2 shows representative sample of the COMs emission, the full sample is shown in Appendix. Three steps of post-processing reduces the image cubes to 1D spectra, which are summarized below.

- Extracting spectra: We use the CASA task `specflux` to extract the mean flux density within the ellipse which has the same major and minor axes as well as the position angle as the fitted continuum sources.
- Baseline calibration: The continuum has been removed before the imaging process; however, the extracted spectra sometimes still show imperfect baselines due to rich emission lines, lack of emission, and broad features. Thus, we manually select the frequency ranges for baseline calibration for each spectral window and each field.
- Velocity correction: Finally, the frequency of the extracted spectra are corrected according to the source velocities. We collect the source velocities from the literature as well as from the strong emission lines in our spectra, such as SO and CS. Table 3 lists the adopted source velocities and the corresponding references.

3.3. *Line Identification and Modeling*

Line identification starts with manual identification and verification for a few sources with rich spectra, including Per-emb-12B and B1-bS. We use SPLATALOGUE[1] to identity the molecular species and use XCLASS (Möller et al. 2017) to verify the identification. The XCLASS package is a LTE radiative transfer code that uses the molecular data from the Cologne Database of Molecular Spectroscopy (CDMS; Müller et al. 2001, 2005; Endres et al. 2016) and the Jet Propulsion Laboratory (JPL; Pickett et al. 1998). An identification needs to satisfy the following criteria.

- The spectra agree with the predicted strengths of the model.
- The spectral lines are not all blended with other emission, such as other molecules and the SiO emission tracing the outflows. The emission of a few species, such as HDCO & $^{13}CH_3OH$, CH_3OH & CH_3OCHO, CH_3CHO & CH_2DOH, ^{34}SO & C_2H_5OH, and CH_3OCH_3 & CH_2DCN, are partially blended (blending occurs at a few lines but other lines remain isolated). The fittings of those species are performed together to verify their identification.
- Identified molecules need to be already found toward young stellar objects as summarized in McGuire (2018).

Table ?? lists the identified species and transitions that are detected in at least one of the PEACHES protostars. Only identifiable transitions are listed. The XCLASS modeling include all the transitions in our frequency coverage for each molecule regardless their Einstein-A values and upper energy levels.

As shown in Figure 2, COMs emission centers around the protostars at $\sim$ 100 $-$ 200 au. At the similar region, the gas density is around $\sim 10^8 cm^{-3}$ (B1-b S: Gerin et al. 2017), similar to the critical density of the COM emission detected in our observations. For example, the CH_3OH line at 243915 MHz has a critical density of $1.4 \times 10^8 cm^{-3}$ (Schöier et al. 2005; Rabli & Flower 2010). Thus, the assumption of LTE holds for modeling the COM emission. YLY: B1-b S is one of the most dense protostars. My guess is that the COMs is close to LTE but not in LTE. We also test the LTE assumption on CH_3OH with the large velocity gradient (LVG) model using RADEX (reference). The column density difference is only X%.

Systematic spectral fitting using XCLASS is applied to all sources using a list of species, compiled from the identifications. Appendix A lists the catalogs used in this study. The fitting function in XCLASS includes several optimization algorithms that can be used in series to reduce biases. We configure the algorithm chain that starts with the genetic algorithm followed by the Levenberg-Marquardt χ^2 minimization. The genetic algorithm searches the best-fitting parameters iteratively with generations that evolve like a natural selection, where the better fitting models get less modification over generations. We setup the genetic algorithm to search for the top two best-fitting models with 30 generations. Then, the Levenberg-Marquardt χ^2 minimization applies to the two best-fitting models for 20 iterations to find the best-fitting models. The genetic algorithm aims

[1] http://www.splatalogue.net/

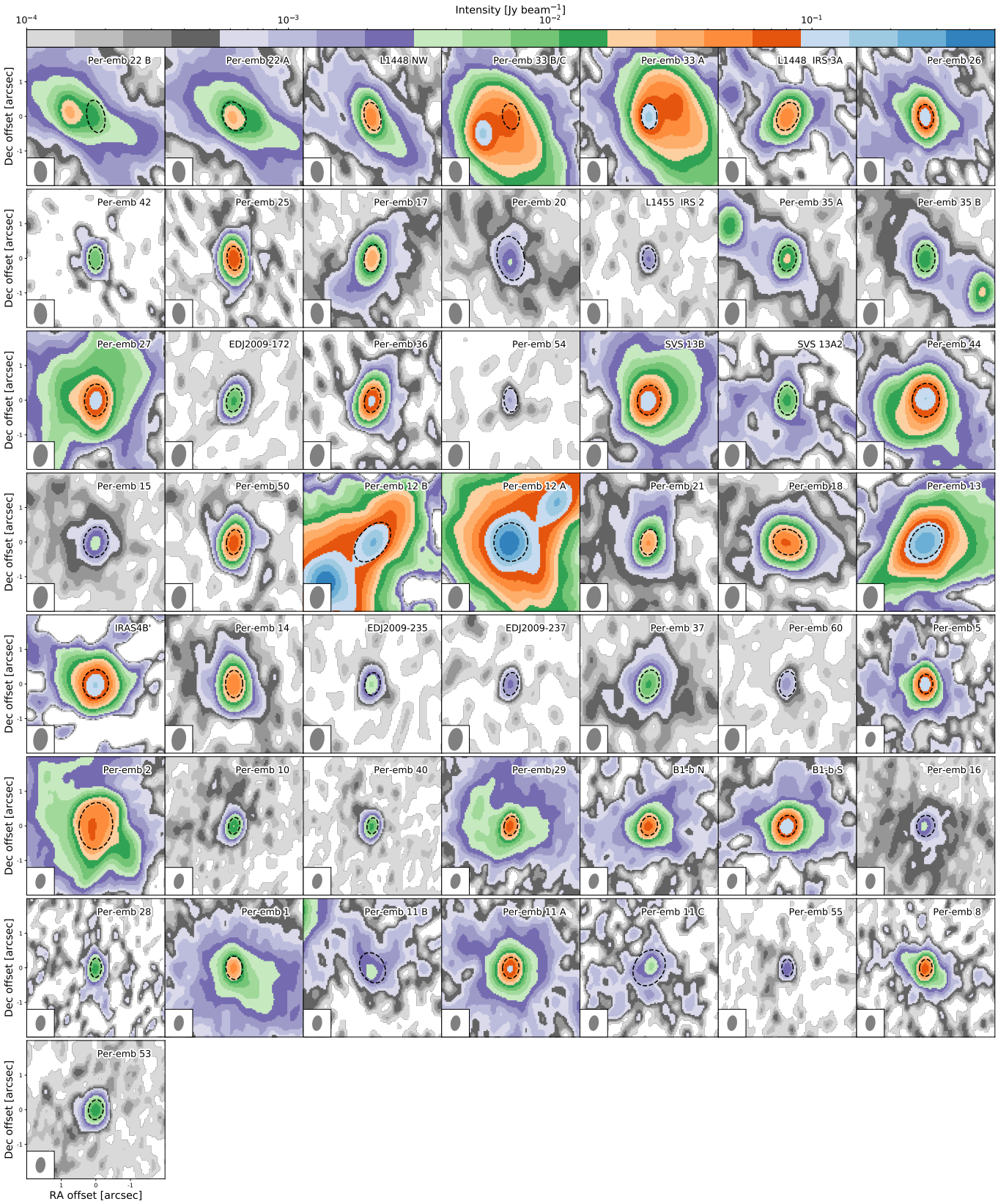

Figure 1. The continuum images of all PEACHES protostars. Non-detections toward L1448 IRS 2E and NGC 1333 SVS 3 are not shown. The dashed ellipses illustrate the size of fitted continuum, which is the region for extracting 1D spectra.

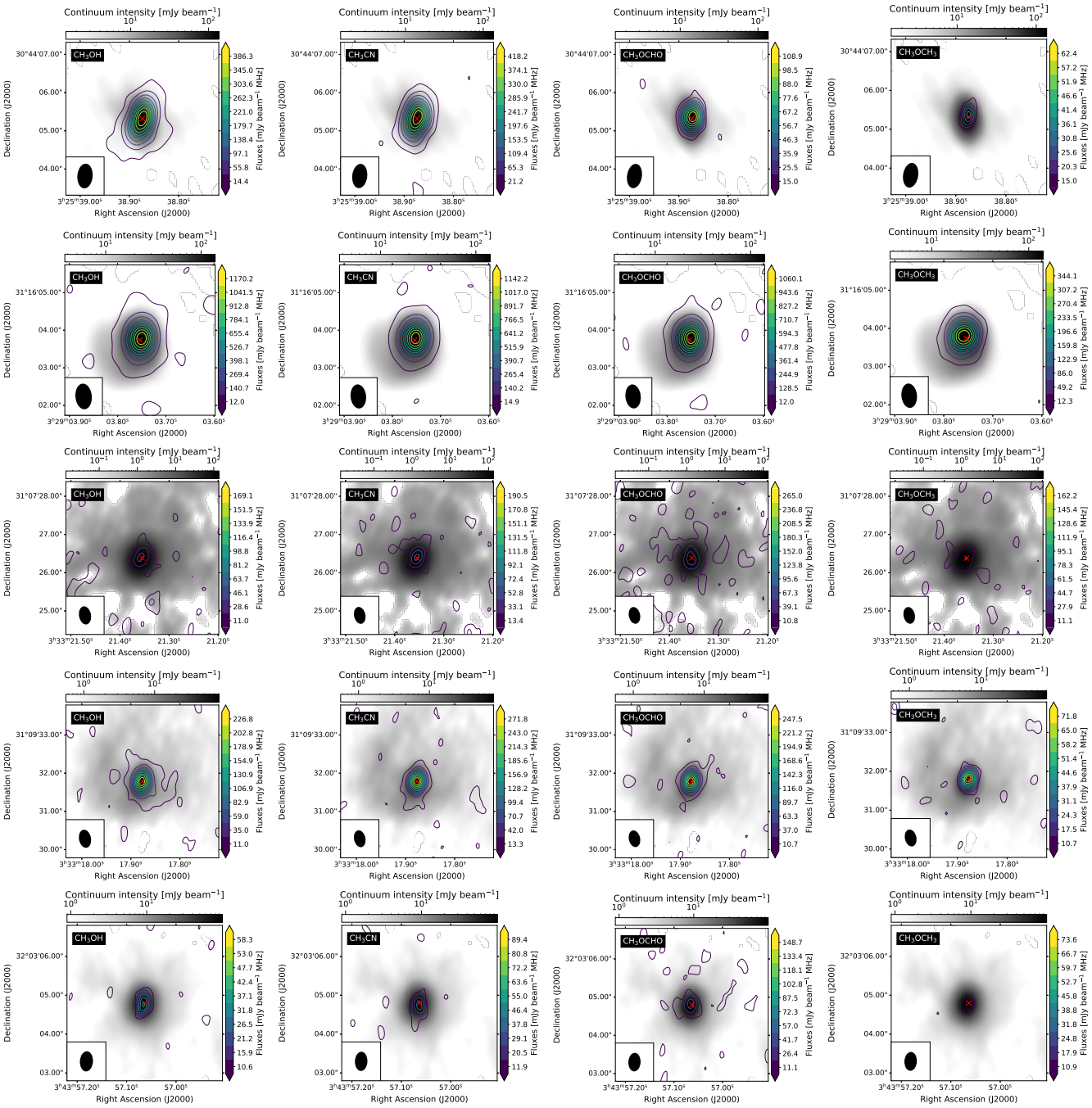

Figure 2. The intensity maps of most detected COMs, CH_3OH, CH_3CN, CH_3OCHO, and CH_3OCH_3 (from left to right). Each row shows the emission from Per-emb 26, Per-emb 44, B1-b S, B1-c, and Per-emb 11 A (top to bottom). The intensity is calculated by integrating over $3\,\mathrm{km\,s^{-1}}$ around the line centroid, while the lowest contour shows the 3σ value. The grayscale images illustrate the continuum emission.

to find local minimums and the Levenberg-Marquardt minimization further finds the best-fitting models in the local minimums. The two best-fitting models found by the genetic algorithm often very similar, suggesting that there is only one minimum. To address the rare cases of two separated local minimums, we pick the model with the lower χ^2 values from the two best-fitting models constrained by the Levenberg-Marquardt minimization.

There are five parameters in the XCLASS modeling, the size of the emitting molecule ($r_{\rm COM}$), the excitation temperature ($T_{\rm ex}$), the column density ($N_{\rm COM}$), the line width ($\Delta\nu$), and velocity offset ($v_{\rm off}$). We assume the COMs are all concentrated at the center, simplified as a 2D thin circular disk. We fix $r_{\rm COM}$ as $0\farcs5$, similar to our beam size, and optimize the model with five excitation temperatures, 100, 150, 200, 250, and 300 K. We allow the line width varying between $1.2\,{\rm km\,s^{-1}}$ to $3.5\,{\rm km\,s^{-1}}$ for better fitting quality but assume no velocity offset from the source velocity, and the allowed range of the column density for each molecule is chosen according to the strength of the emission. From the fitting results of five $T_{\rm ex}$, if a molecule is detected, the mean column densities will be the best-fitting column density, while the range of the column densities indicates the upper and lower uncertainties. If a molecule is non-detection, the synthetic spectra for all lines are scaled to match the peaks of the each line fitted by a Gaussian profile. Then, we take the minimum of the corresponding column densities as the upper limit.

4. RESULTS

4.1. *Detection Statistics*

We summarize the detection statistics in Figure 3, which includes COMs, the carbon-chain molecules, and the simple organic molecules, such as CS, $H^{13}CN$, SO, ^{34}SO, and SO_2. In the following results of detection fraction, we include the three sources that are excluded from modeling due to no reliable source velocity, making a total of 50 sources. The COMs discussed here are the derived from the spectra taken toward the continuum peak (Section 3.1). We focus on the chemistry of COMs in the disk-forming regions in this study, therefore, excluding detection of molecules outside the continuum peak. A comparison of chemical composition in protostellar envelopes (100–1000 au) requires observations with larger maximum recoverable scale ($\theta_{\rm MRS}$).

The PEACHES protostars show a great chemical diversity from no molecule detected (e.g., B1-bN and L1455 IRS 2) to rich spectra of COMs (e.g. Per-emb 13). Most of the PEACHES protostars have simple organics, such as SO, CS, $H^{13}CN$, and HDCO, and $\sim 60\%$ of sources have SO_2 and ^{34}SO. Emission of C_2H can be easily identified from the spectra. However, the C_2H toward the continuum sources often shows irregular line profiles together with velocity offsets and absorption (Figure 14). In fact, warm environments, such as the outflow cavity wall, easily enhance the abundance of C_2H because of elevated abundance of C^+ (e.g., Zhang et al. 2018; Imai et al. 2019). Thus, C_2H emission is extended along with the outflow cavities, making the 1D spectra toward the continuum source unrepresentative. Observations with a larger $\theta_{\rm MRS}$ will provide a complete representation of the C_2H abundance on the inner envelope.

Several sources have their SiO emission with a broad line width, significantly contaminating the emission of CH_3CH_2CN and CH_3CHO. In the later quantitative discussion, we exclude the spectral windows contaminated by the SiO emission. For assigning the detections, we can distinguish the emission of CH_3CH_2CN and CH_3CHO from the broad SiO emission in a few sources, such as CH_3CHO in Per-emb 26.

Figure 4 shows the number of COMs detected toward the PEACHES sample. Twenty-one (45%) sources have no COMs detected. CH_3OH is detected in 28 sources (56%); CH_3OCHO is detected in 15 sources (32%); and N-bearing COMs are detected in 20 sources (40%). Comparing to the COMs in the CALYPSO survey (Belloche et al. 2020), the fraction of sources that have methanol, $\sim$50%, is similar to that for the PEACHES protostars. Also, 30% of the CALYPSO sources have at least three COMs, while 28% of the PEACHES protostars have at least three COMs.

We compare the number of detected COMs with the bolometric luminosity ($L_{\rm bol}$), the bolometric temperature ($T_{\rm bol}$), and the dust mass estimated by Tychoniec et al. (2020) using observations at 9 mm ($M_{\rm central}$). The number of COMs shows no obvious trend with $L_{\rm bol}$, $T_{\rm bol}$, and $M_{\rm central}$. For $L_{\rm bol}$, the sources with at least three COMs all have $L_{\rm bol} \gtrsim 3\,{\rm M_\odot}$, except for B1-b S. However, the sources without any COMs also have a similar $L_{\rm bol}$. If COMs mostly come from thermal desorption, the region with $T > T_{\rm desorption}$ may be smaller for the low luminosity sources, making the emission of COMs fainter and reducing our sensitivity to detect COMs. The COM-rich sources have $T_{\rm bol}\sim 50\,{\rm K}$, while the COM-poor sources have a greater scatter of $T_{\rm bol}$, ranging from 14.7 K to 1100 K. The protostars with high $M_{\rm central}$ ($>666.5\,{\rm M_\oplus}$) have detections of COMs. However, the protostars with low $M_{\rm central}$ can have either many COMs or no COM.

The sources with high continuum brightness temperature ($T_{\rm b}$) tend to have rich spectra COMs (Figure 5), while the sources with no detection of COM have their

Table 4. Rotational Temperatures of Methanol

Source	$T_{\rm rot}$
Per-emb 26	$120.1^{+2.6}_{-2.5}$ K
Per-emb 22 A	$182.4^{+11.2}_{-11.4}$ K
Per-emb 22 B	$157.5^{+13.4}_{-13.0}$ K
Per-emb 17	$173.9^{+1.8}_{-1.9}$ K
Per-emb 44	$197.5^{+0.3}_{-0.3}$ K
Per-emb 12 B	$194.0^{+0.8}_{-0.8}$ K
Per-emb 13	$208.6^{+3.9}_{-4.0}$ K
Per-emb 27	$195.8^{+0.4}_{-0.4}$ K
Per-emb 21	$151.0^{+14.6}_{-15.6}$ K
Per-emb 35 A	$145.1^{+3.7}_{-3.7}$ K
Per-emb 18	$395.7^{+30.7}_{-30.4}$ K
B1-bS	$241.7^{+11.7}_{-11.9}$ K
Per-emb 29	$227.7^{+3.2}_{-3.3}$ K

$T_{\rm b}\lesssim$10 K. The brightest source in continuum, Per-emb 12 A has many molecules detected in absorption due to the high continuum opacity blocking the emission of COMs (Sahu et al. 2019; De Simone et al. 2020). The continuum brightness temperature traces the gas column density, tracing the amount of embedding gas around the protostars. Thus, the tendency between many COMs and the high $T_{\rm b}$ hints the scenarios where the denser envelope either increases the detectability of COMs or enhance the complexity of molecules.

Compact emission of COMs suggests ...

5. COLUMN DENSITIES

5.1. *Excitation Temperatures*

The PEACHES spectra cover four methanol lines, while the spectra of each source include three of them due to the frequency shift in the wide spectral window. The three methanol lines have upper energy ranging from ∼50 K to ∼500 K, which allows us to estimate the rotational temperature of methanol if all three lines are detected. To construct the methanol rotational diagram, we fit the methanol emission with a Gaussian profile and bootstrap the measurements for fitting the rotational temperature. Figure 6 shows the rotational diagram of Per-emb 22 B along with the sampled rotational temperature. The derived rotational temperature of methanol ranges from 120 K to 240 K with an exception of Per-emb 18, which has a rotational temperature of 395.7 K for methanol (Table 4).

YLY: need to redo the MCMC fitting. The fitting shown here is 6 months old. For the sources with significant emission of CH_3OCHO, the column density and the excitation temperature of CH_3OCHO can be constrained with MCMC. Table 5 lists the sources where the MCMC fitting is feasible and the derived properties of CH_3OCHO. The best-fitting temperatures range from 100-300 K with a few outliers at ∼1000 K. The spectra with the high excitation temperature show non-Gaussian line profiles, making the fitting inaccurate. Therefore, we exclude those sources in Table 5.

[put the derived values from HCOOCH3 for several sources. and say consistency with several other works.] [Put the discussions in 6.1.1. in your section number, and say consistency with HCOOCH3]. [say the assumption/justification of T for sources without multiple line detections(i.e. sources, which is difficult to derive T). It could partly be overlapped with the section 3.2 (3.1 in your numbering)]

5.2. *Correlations of COMs*

The chemical evolution of protostars may leave certain patterns in the abundance of molecules as the dynamical evolution determines the density and temperature structures, which regulate chemical reactions. Thus, the abundance of COMs and their correlations provide critical information to constrain the chemical evolution at embedded protostars.

As described in Section 3.3, we fit the column density and line width with different excitation temperatures, resulting in a range of column density as its uncertainty. To quantify the goodness of correlation, we calculate the Pearson's correlation coefficient (r), which tests the linearity of two variables. A simple calculation of the Pearson's correlation coefficient would ignore the uncertainties of the column density. Thus, we use the bootstrapping method to sample the fitted column densities to calculate Pearson's r, by assuming a normal distribution centers on the best-fitted values with the uncertainty as the width of the normal distribution. If we include the upper limits as normal distributions center on zero, the correlation coefficient becomes significantly lower due to the cluster of samples around zero column density (Figure 8). With the detection-only sample, the mean Pearson's r_d is 0.91, as expected for a tight correlation, with a Gaussian-like distribution skewed toward lower values. After including the upper limits, the mean Pearson's r decreases to 0.59 with larger uncertainty (the 68% credible interval increases by 160%). Thus, the bootstrapped correlation coefficient only considers the detections.

Figure 9 shows the correlations of several COMs selected from their detection rates. The column density of CH_3OH best correlates with that of CH_3CN. Belloche et al. (2020) also found the tight correlation between these two molecules from the CALYPSO survey, which has a selective sample. The column densities of

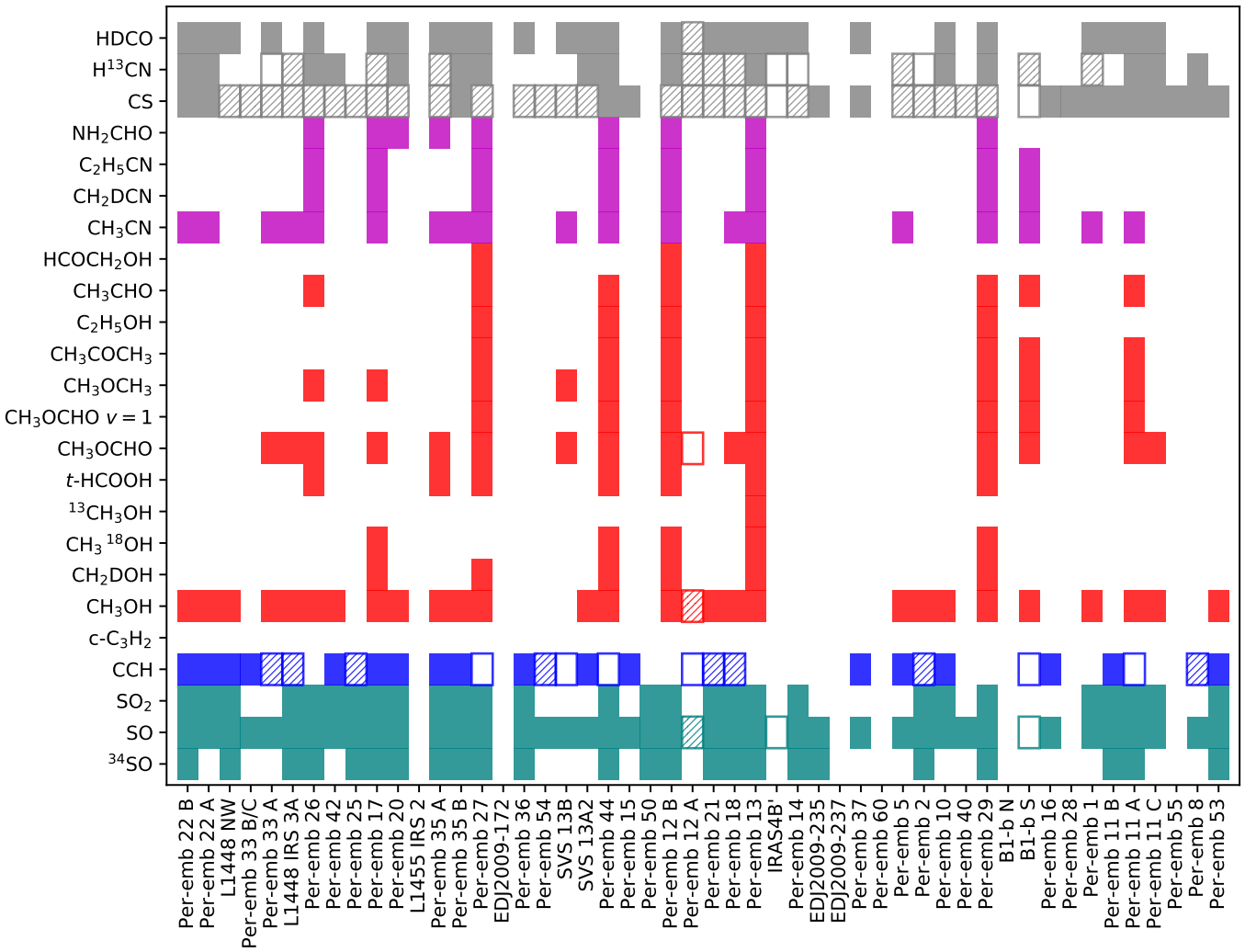

Figure 3. Summary of molecular detections. The sources are sorted by increasing R.A. from left to right. The detections are color-coded by the types of species: S-bearing molecules in green, carbon-chain molecules in blue, O-bearing COMs in red excluding N-bearing molecules, N-bearing COMs in magenta, other simple organics in gray. The boxes with solid colors indicate emission and the empty boxes indicate absorption. The hatched boxes indicate both emission and absorption are seen.

CH_3OCH_3 and CH_3OCHO also show a tight correlation. CH_3OH also correlates with more complex species (i.e. so called daughter species, CH_3OCHO and CH_3OCH_3) with a lower correlation coefficient than that between CH_3OH and CH_3CN. The correlations between CH_3CN and more complex species also show the same behavior. The decreasing strength of correlation with between the simple COMs and more complex COMs supports the hypothesis that CH_3OH and CH_3CN are first generation species and CH_3OCHO and CH_3OCH_3 are the second generation (reference).

While the column density shows

To confirm this correlation, we have also prepared normalized correlation plots. [explain the method, and meaning of the normalization] Similar values of the correlation coefficient are obtained.

Averaged abundance ratios are also summarized in the plot.

For other COMs detected in this survey, the correlation plots are shown in Figure XX.

The number of detected sources are not enough to discuss the difference in correlation coefficient (less than 10 points??). However, marginal correlations could be seen. Abundance ratios are discussed in section XX. [please add the ratios.]

6. DISCUSSION

6.1. *Hot Corinos*

6.2. *Chemical Difference among Hot Corinos*

Among hot corino sources, no tight correlations are seen as well (FigureXX). [explain the plots] On the other hand, when we take relative abundance to CH3OH,

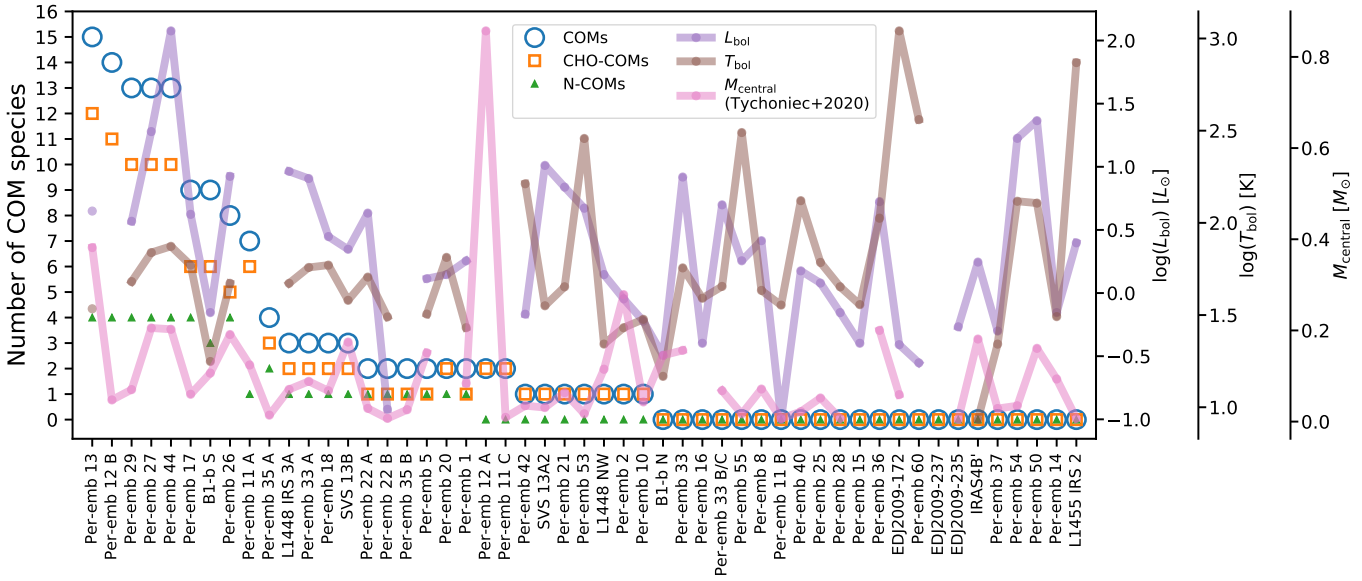

Figure 4. The number of COMs detected toward the PEACHES sources compared with the bolometric luminosity (purple), the bolometric temperature (brown), and the central dust mass (pink, Tychoniec et al. (2020)). The sources are sorted by the total number of COMs with the number of O-bearing COMs, N-bearing COMs, and all COMs labeled as orange boxes, green triangles, and blue circles, respectively. The mass of unresolved systems is estimated as the sum of each protostar. The bolometric luminosities and the bolometric temperatures are taken from Tobin et al. (2016) and Murillo et al. (2016).

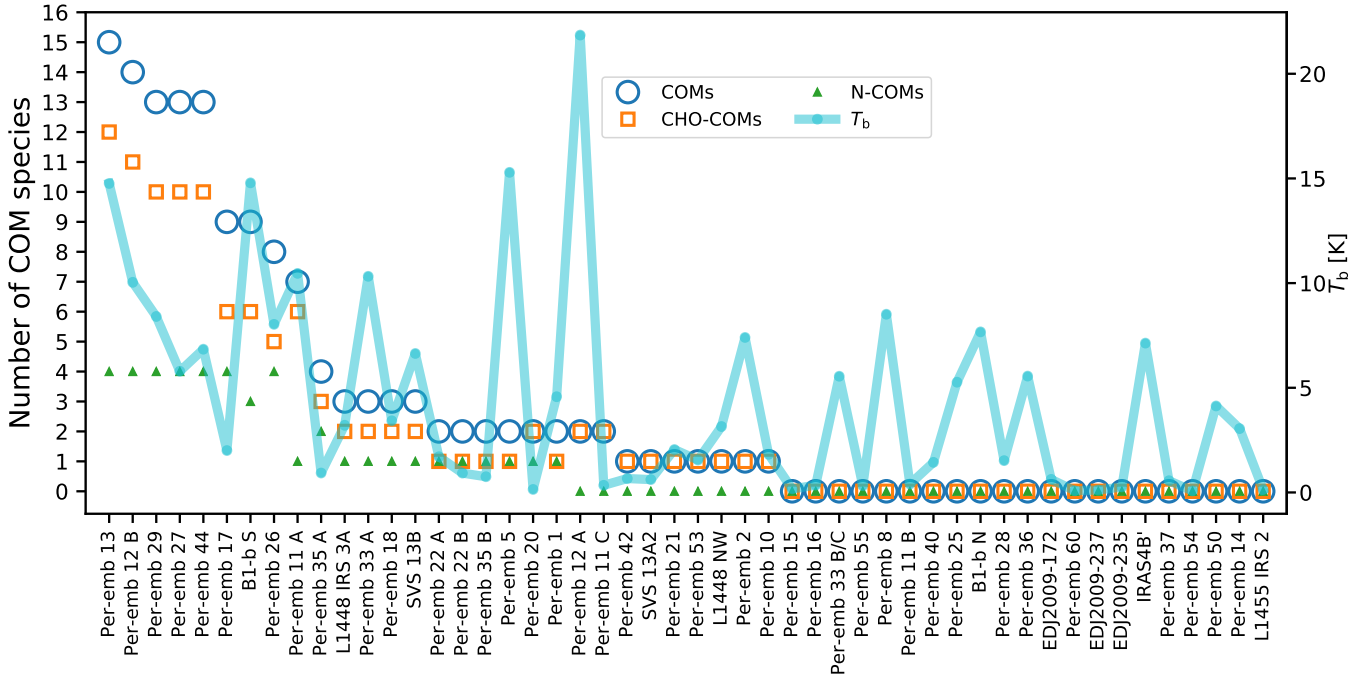

Figure 5. The number of COMs detected toward the PEACHES sources compared with the continuum brightness temperature. The legends for the protostars are the same as Figure 4. The brightness temperatures are indicated in green.

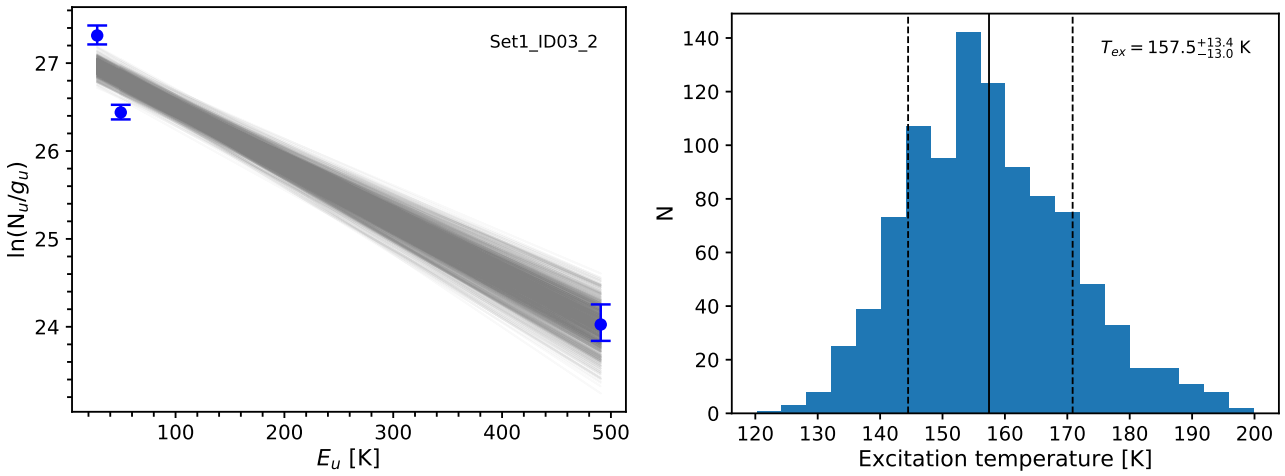

Figure 6. The methanol rotational diagram for Per-emb 22B and the fitted excitation temperature distribution using the bootstraping method.

Table 5. MCMC Fitting of Methyl Formate

Source	Temperature [K]		$\log(\mathcal{N})$ [cm^{-2}]		Line width [km s^{-1}]	
	best	mode±HPD	best	mode±HPD	best	mode±HPD
Set1_ID01_2	95	76^{+315}_{-56}	15.24	$15.29^{+0.42}_{-0.42}$	4.86	$4.77^{+0.22}_{-0.52}$
Set1_ID02	87	98^{+14}_{-41}	15.67	$15.67^{+0.10}_{-0.08}$	3.66	$4.06^{+0.65}_{-0.79}$
Set1_ID06	93	93^{+59}_{-35}	15.67	$15.67^{+0.12}_{-0.08}$	4.84	$4.77^{+0.22}_{-0.02}$
Set2_ID00	263	310^{+3}_{-56}	16.89	$16.92^{+0.05}_{-0.04}$	3.95	$3.95^{+0.15}_{-0.12}$
Set2_ID01_2	217	194^{+75}_{-4}	16.37	$16.36^{+0.10}_{-0.03}$	2.22	$2.25^{+0.14}_{-0.12}$
Set2_ID02	195	225^{+119}_{-64}	16.04	$16.10^{+0.20}_{-0.09}$	1.21	$1.21^{+0.00}_{-0.01}$
Set2_ID07	152	131^{+281}_{-120}	14.79	$14.72^{+0.53}_{-0.43}$	3.24	$1.66^{+2.26}_{-0.40}$
Set2_ID08	159	10^{+551}_{-0}	14.75	$14.11^{+0.85}_{-0.04}$	2.37	$1.20^{+2.15}_{-0.00}$
Set2_ID12	115	41^{+269}_{-30}	14.96	$15.02^{+0.05}_{-0.94}$	4.54	$4.89^{+0.09}_{-1.70}$
Set3_ID00	98	58^{+41}_{-14}	15.85	$15.82^{+0.26}_{-0.09}$	1.24	$1.25^{+0.02}_{-0.05}$
Set3_ID01	134	134^{+13}_{-27}	16.59	$16.60^{+0.02}_{-0.02}$	3.04	$3.08^{+0.18}_{-0.15}$
Set3_ID07	104	92^{+182}_{-45}	15.67	$15.67^{+0.29}_{-0.15}$	2.44	$2.33^{+1.22}_{-0.66}$

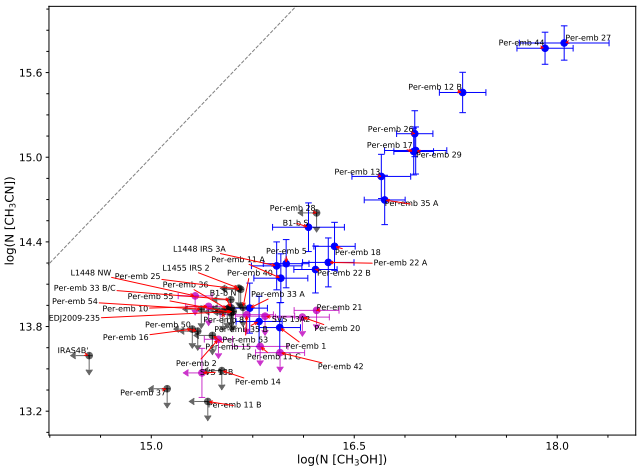

Figure 7. Correlation of the fitted column densities of CH_3OH and CH_3CN from the PEACHES protostars. The sources where both molecules are detected are shown in black; the sources where only one molecule is detected are shown in magenta; finally, the sources where both molecules are not detected are shown in black for the corresponding upper limits.

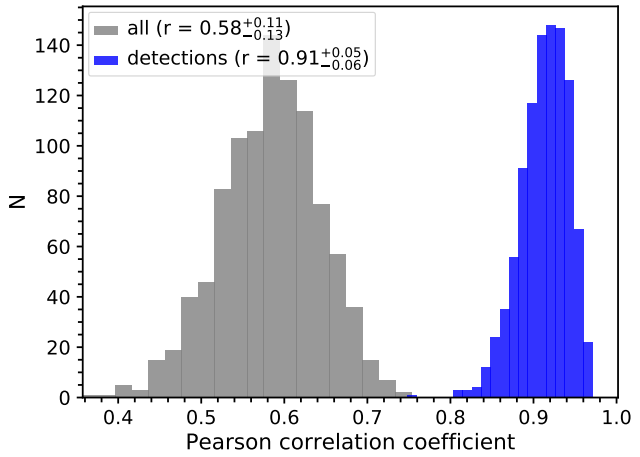

Figure 8. Distributions of Pearson's correlation coefficient from 10000 resamples drawn from detections + non-detections and only detections. The legend indicates the mean values of Pearson's r along with the range of the 95% credible interval as the associated uncertainties.

marginal trend could be seen in correlation between Tcont. [explain what you presented in the talk. more complex species may require higher density?]

6.3. *O-bearing and N-bearing COMs*

- perfect correlation between CH3OH and CH3CN -¿ both could be 1st generation species. No significant difference between o-bearing and N-bearing abundances among the YSOs in perseus. (at least, elemental abundance could be almost the same since our samples are in the same cloud complex.)

- [please mention about abundance ratios C2H5CN, NH3CHO vs CH3OCH3 and CH3OCHO. and refer several papers discussed the O- and N difference. such as in Orion KL and/or IRAS16293???] O- and N- difference might be enhanced in more complex species (?).

6.4. *Origin of the CH_3OH/CH_3CN Correlation*

- CH3OH formation is well known(surface hydrogenation)

- explain hypothesis and possible expectations of CH3CN formation[see my e-mails]

7. CONCLUSION

Y.-L. Yang acknowledges the supports the JSPS Postdoctoral Fellowship from Japan Society for the Promotion of Science. This paper makes use of the following ALMA data: ADS/JAO.ALMA#2016.0.00391.S. ALMA is a partnership of ESO (representing its member states), NSF (USA) and NINS (Japan), together with NRC (Canada), MOST and ASIAA (Taiwan), and KASI (Republic of Korea), in cooperation with the Republic of Chile. The Joint ALMA Observatory is operated by ESO, AUI/NRAO and NAOJ. The National Radio Astronomy Observatory is a facility of the National Science Foundation operated under cooperative agreement by Associated Universities, Inc.

Facilities: ALMA

Software: astropy, XCLASS, spectral-cube, CASA

APPENDIX

A. CATALOGS FOR MOLECULAR DATA

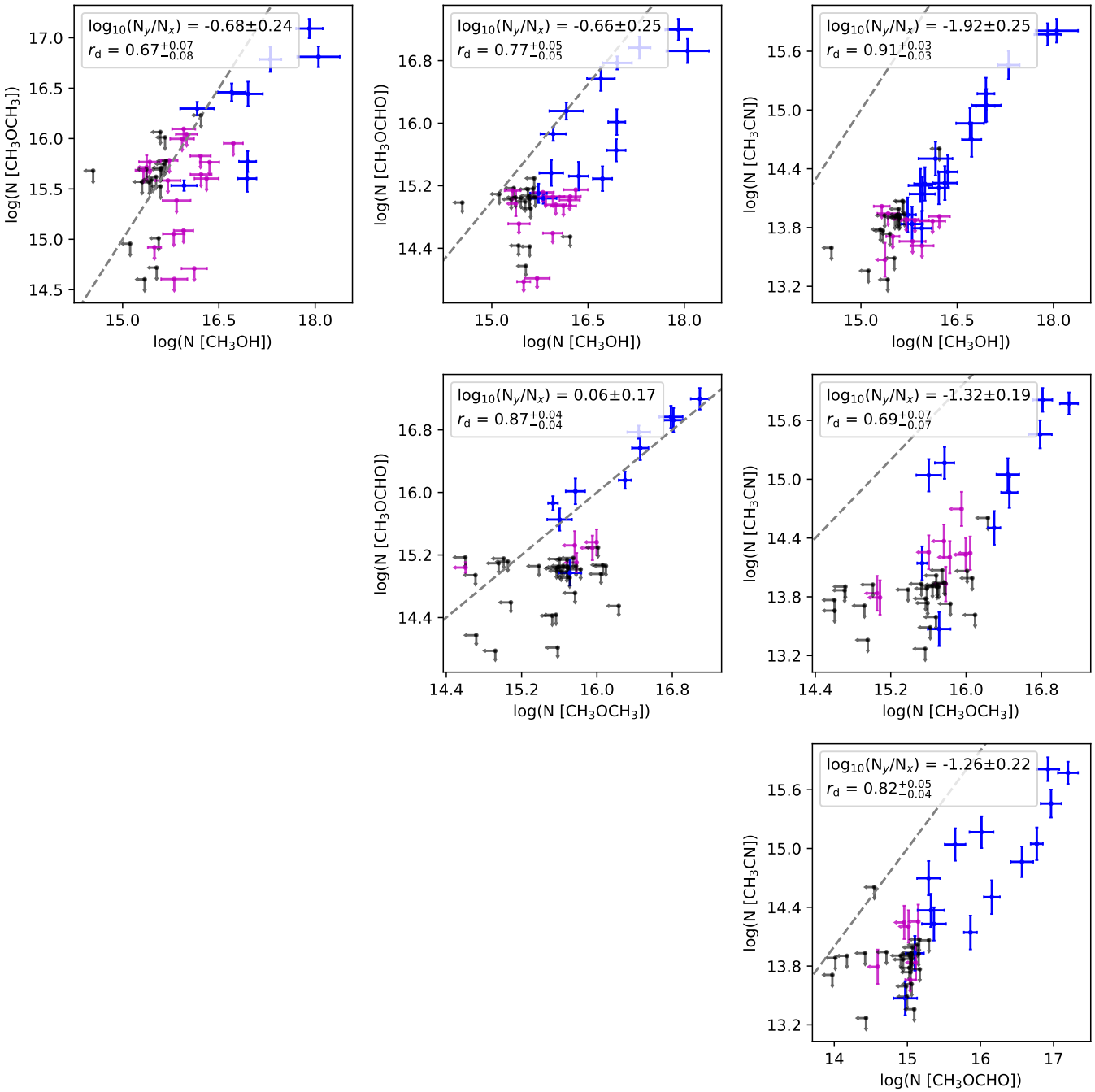

Figure 9. Corner plot of the correlations of the column densities between CH_3OH, CH_3CN, CH_3OCHO, and CH_3OCH_3. The color code follows that in Figure 7. The dashed line indicates equality. The legends indicate the Pearson's r for the detection-only sample (r_d) and the logarithmic ratio of the two molecules (N_y/N_x). The four most detected COMs are shown in this figure, while other COMs are shown in Figure 11.

B. IDENTIFIED SPECIES AND TRANSITIONS

Table **??** lists the species and their transitions identified from the PEACHES spectra.

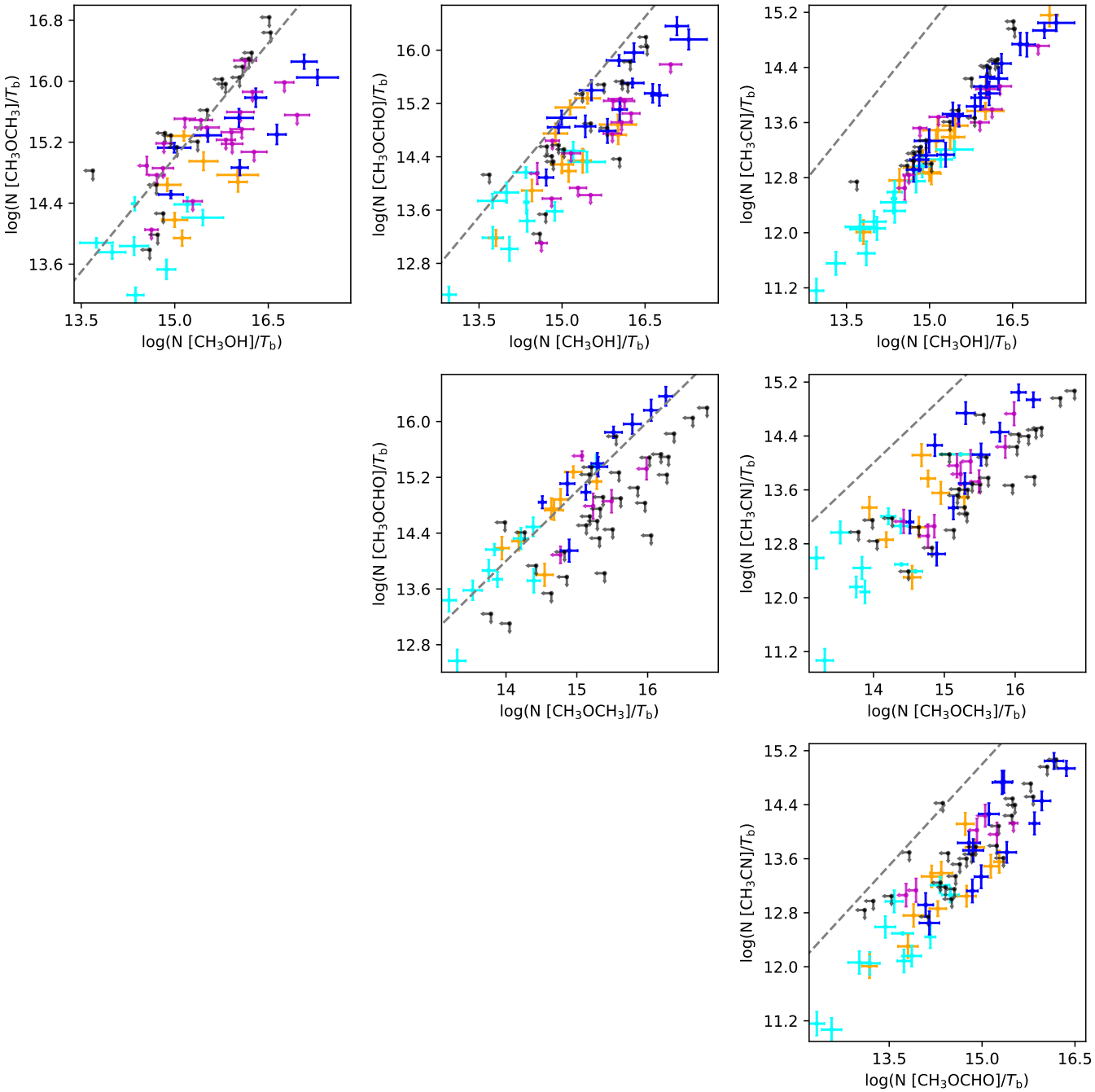

Figure 10. Corner plot of the correlations of the normalized column densities. The blue, magenta, and black symbols indicate the column densities normalized by the continuum brightness temperature ($T_{\rm b}$), while the color scheme follows that in Figure 7. The orange symbols show the column densities normalized by $T_{\rm b}$ and the bolometric luminosity ($L_{\rm bol}$), while the cyan symbols show that normalized by $T_{\rm b}$ and the bolometric temperature ($T_{\rm bol}$). We only show the column densities if both molecules are detected for the ones normalized by $T_{\rm b}T_{\rm bol}$ and $T_{\rm b}L_{\rm bol}$. A few close multiple sources, including Per-emb 12 A & B, Per-emb 35 A & B, and Per-emb 11 A & C, are excluded for the normalization of $T_{\rm bol}$ and $L_{\rm bol}$ due to their poorly determined SEDs.

C. INTENSITY MAPS OF CH_3OH, CH_3CN, CH_3OCHO, AND CH_3OCH_3

D. THE SPECTRA OF C_2H

The C_2H spectra toward the continuum emission have irregular line profiles. Some spectra have strong self-absorption, while some spectra only show the blue-shifted emission. Due to the absorption and irregular line profile,

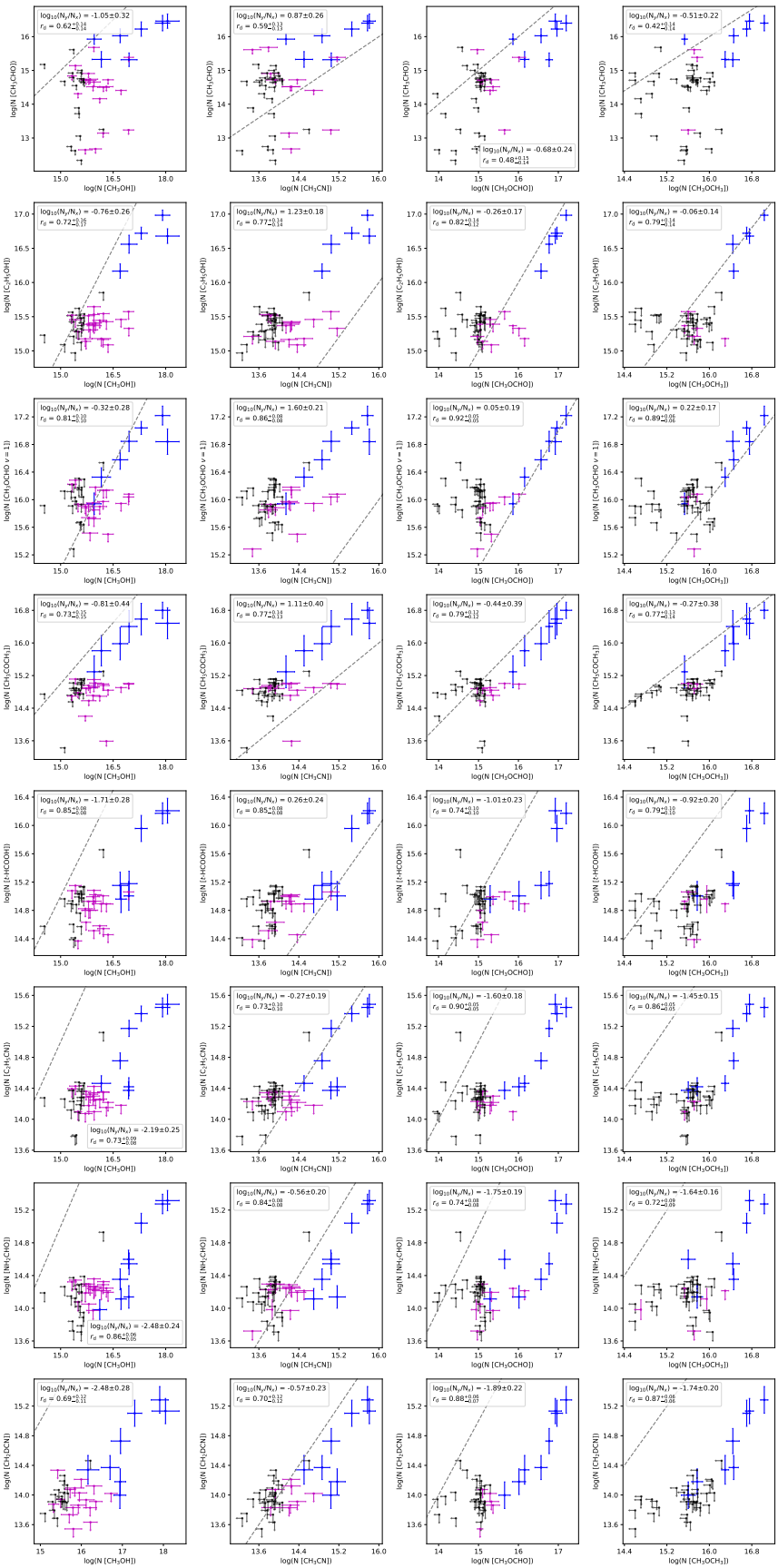

Figure 11. Corner plot of the correlations of the column densities between the more abundance COMs, CH_3OH, CH_3CN, CH_3OCHO, and CH_3OCH_3, and the less abundance COMs CH_3CHO, C_2H_5OH, CH_3OCHO $v = 1$, CH_3COCH_3, CH_3CH_2CN, t-HCOOH, and NH_2CHO. The legends are similar to Figure 7.

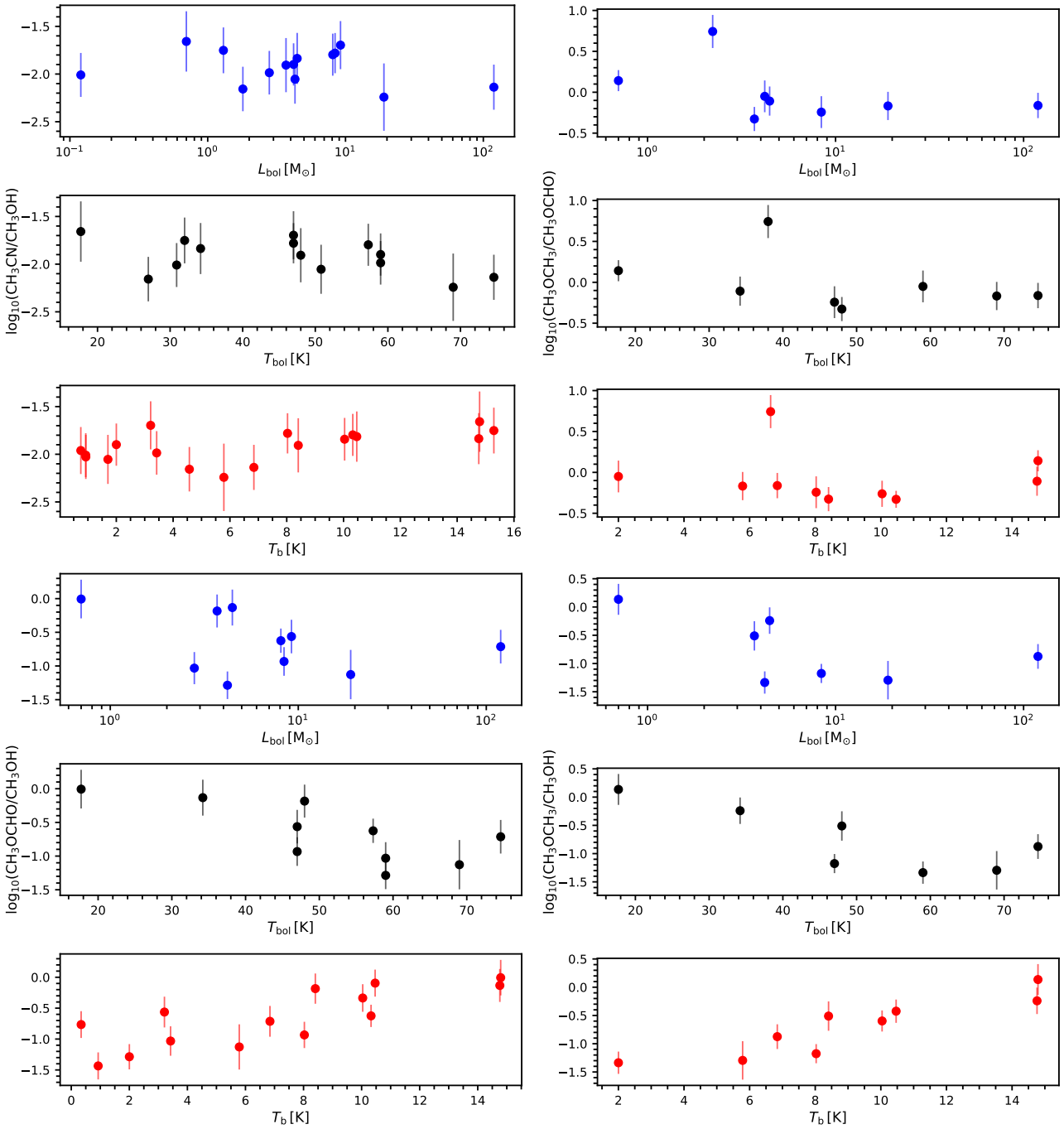

Figure 12. Ratios of well-detected molecules, CH_3OH, CH_3CN, CH_3OCHO, and CH_3OCH_3, as functions of $L_{\rm bol}$ (blue), $T_{\rm bol}$ (black), and $T_{\rm b}$ (red).

the XCLASS fitting routine often fails to faithfully reproduce the observed C_2H spectra. C_2H can easily form in the outflow cavity wall due to the abundant CH_4 sublimated from dust grains as well as C^+ ionized by the UV radiation. Thus, the C_2H spectra can have broad line width and multiple components. Furthermore, the morphology of the C_2H emission traces the outflows, making our extraction from the continuum emission non-ideal for representing the nature of the C_2H emission. Figure 14 and Y show the spectra and the moment 0 map of C_2H, respectively.

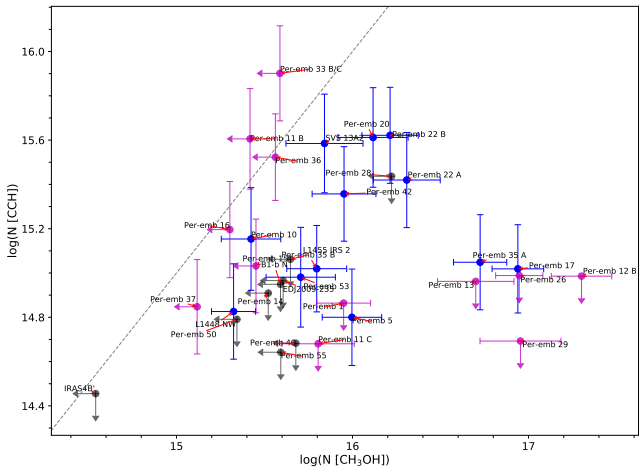

Figure 13. Correlation of the column densities of C_2H and CH_3OH fitted from the PEACHES protostars. The sources where both molecules are detected are shown in black; the sources where only one molecule is detected are shown in magenta; finally, the sources where both molecules are not detected are shown in black for the corresponding upper limits.

E. NOTES ON THE COMS MODELING

F. NOTES ON THE 1D SPECTRA

Per-emb-33-A—

- The fitting of CH_3OCHO reproduces the the strongest emission at 259343 MHz, but underestimates the emission between 246275 MHz to 247070 MHz, where the emission is at most 0.5 K. Considering the narrow absorption in HCN, CS, and SO lines as well as the brighter continuum temperature (10.5 K), the emission of CH_3OCHO may be affected by the continuum opacity.

Per-emb-26—

- Red-shifted excess appears in the CH_3OH lines.
- Unidentified lines at 246525 MHz and 244249 MHz.

Per-emb-17—

- Many line profiles exhibit a broad double-peaked profile, separated by $\sim$5–6 $\mathrm{km\,s^{-1}}$. Per-emb-17 is a binary system unresolved by our observations. However, the channel maps suggest that the two components are likely to surrounding the southern source, Per-emb-17-B.
- The CH_3OCHO line at $\sim$259343 MHz may be optically thick.

SVS13 A2—

- Weak indication of the unidentified line at 246525 MHz, which has been detected in other sources.

Per-emb-44—

- Unidentified lines at 244248 MHz, 246219 MHz, 246254 MHz, 246344 MHz, 246389 MHz, 246434 MHz, 246525 MHz, 246838 MHz, 258268 MHz, 258271 MHz, and 262068-262070 MHz.
- Higher temperatures (Tex >100 K) provide better fittings. Probably should adopt the temperature fitted from CH_3OCHO (previous MCMC fitting suggests a temperature of 263 K).

Per-emb-12-B—

- Unidentified lines at 244248 MHz, 246254 MHz, 246314 MHz, 246322 MHz, 246389 MHz, 246434 MHz, 246525 MHz, 246696 MHz, 246838 MHz, 246873 MHz, 247082 MHz, 258268 MHz, 258271 MHz, and 262068-262070 MHz.

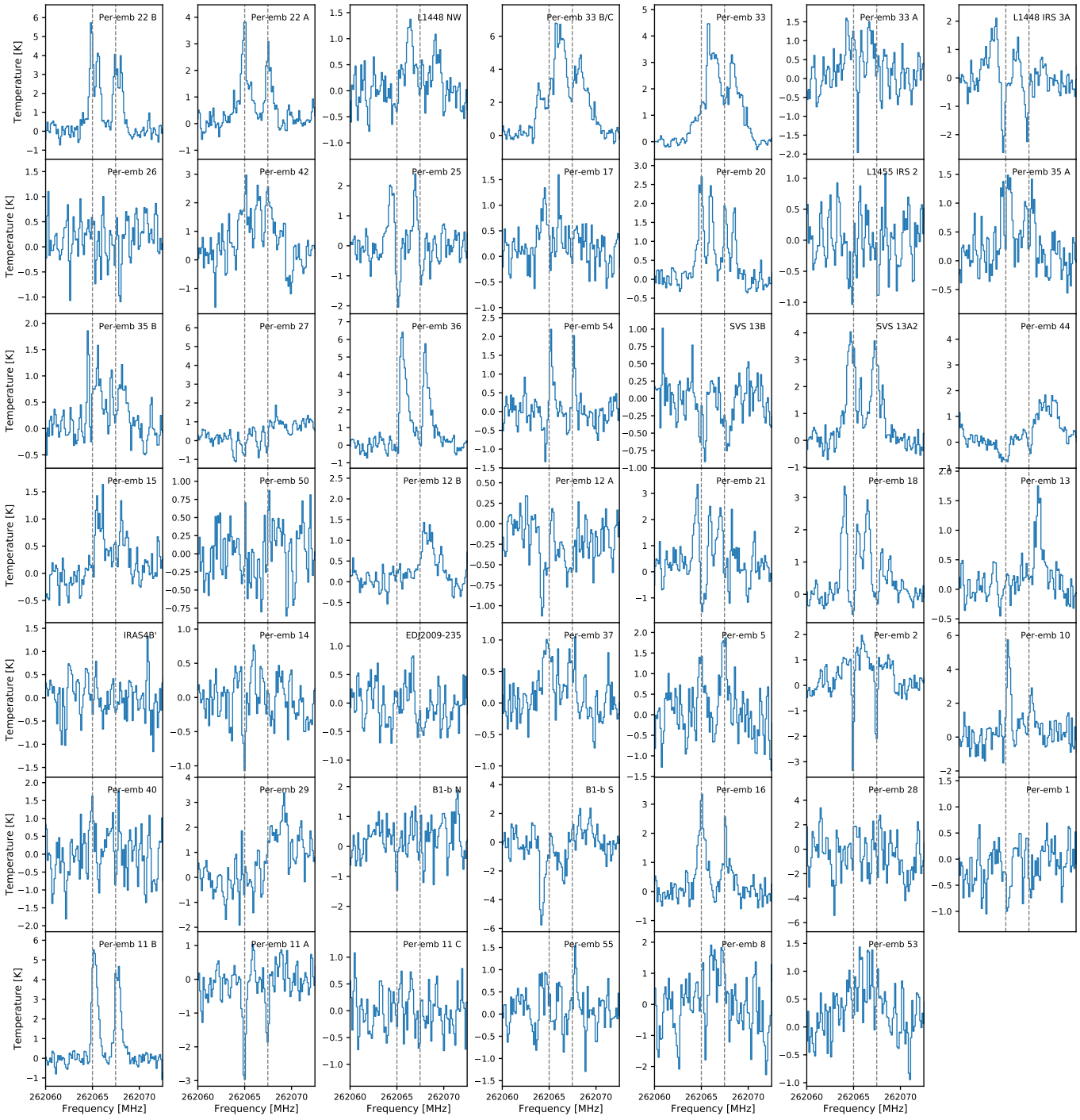

Figure 14. The C_2H spectra of all PEACHES sources extracted from the continuum emission.

Per-emb-12-A —

- Strong absorption features detected across the spectra, CCH, SO, $H^{13}CN$, CS, CH_3OH, HDCO, CH_3CN, and CH_3OCHO.

IRAS4B' —

- Spectra show no emission along with absorption at SO, CS, and CH_3OH lines.

Per-emb-13—

- The CH_3OCHO emission needs T_{ex} >100 K to have a good fit.
- All three CH_3OH lines are detected but two of them show clear sign of self-absorption, therefore, not ideal for fitting the excitation temperature.
- Unidentified lines at 244248 MHz, 246254 MHz, 246331 MHz, 246344 MHz, 246434 MHz, 246525 MHz, 246838 MHz, 246974 MHz, 247086 MHz, 257268 MHz, 257271 MHz, 259323 MHz, 259331 MHz, 262098 MHz, and 262109 MHz.
- The best-fitting model for $^{13}CH_3OH$ lines overestimates the line width due to the weak and broad line at 247086 MHz.

Per-emb-27—

- All three CH_3OH lines are detected, but none of the temperature produce a good fit to all three lines, suggesting that some lines are optically thick. The intensities of the transitions at 243916 MHz and 261806 MHz are ∼30 K, while the intensity at 246873 MHz is about 24 K. They seems to be optically thick. In comparison, the continuum brightness temperature is only 5.8 K.
- Unidentified lines at 244232 MHz, 244248 MHz, 246207 MHz, 246254 MHz, 246388 MHz, 246435 MHz, 246525 MHz, 246538 MHz, 246838 MHz, 246973 MHz, 247084 MHz, and 259330 MHz.
- The CH_3OH line at 243916 MHz and the SO lines become optically thick at 100 K.

Per-emb-21—

- Emission of CH_3OH is detected. However, the broad width and noisy spectra lead to a bad fit. The best-fitting model has the maximum line width allowed, 3.5 km s^{-1}.

Per-emb-35-B—

- The CH_3OH line at 243915 MHzhas an S/N of 1.2, but hints the existence of CH_3OH.

Per-emb-35-A—

- The goodness of fitting for the CH_3OH lines is a strong function of temperature, suggesting that the CH_3OH lines can indicate the T_{ex}.
- The CH_3OCHO line at 259342 MHz has an S/N of 1.8, but hint the existence of CH_3OCHO.

Per-emb-15—

- All lines have only the blue-shifted emission, making them blue-asymmetric.

Per-emb-18—

- Many transitions of CH_3OCHO are tentatively detected; however, none of them has S/N > 3. Currently categorized as non-detection.

B1-bS—

- Higher temperatures produce worse fittings to the CH_3OCHO lines. Previous MCMC fitting of the CH_3OCHO lines suggests a temperature of 58 K.
- The fitting of CH_3OCH_3 is limited by the minimum line width of 1.2 km s^{-1}.
- Unidentified lines at 246027 MHz, 246099 MHz, 246143 MHz, 246192 MHz, 246525 MHz, 246674 MHz, and 2467320 MHz.
- The CH_3OCHO lines around 258278 MHz and the $H^{13}CN$ lines have a few dips within the line profile, suggesting absorption or just noisy spectra.

Per-emb-29—

- Only two CH_3OH lines are covered. Both lines have a strength of ∼10 K, suggesting optically thick.

REFERENCES

Aikawa, Y. 2013, Chemical Reviews, 113, 8961

Belloche, A., Maury, A. J., Maret, S., et al. 2020, A&A, 635, A198

Bergner, J. B., Öberg, K. I., Garrod, R. T., & Graninger, D. M. 2017, ApJ, 841, 120

Bottinelli, S., Ceccarelli, C., Williams, J. P., & Lefloch, B. 2007, A&A, 463, 601

Bottinelli, S., Ceccarelli, C., Lefloch, B., et al. 2004, ApJ, 615, 354

Carney, M. T., Yıldız, U. A., Mottram, J. C., et al. 2016, A&A, 586, A44

Cazaux, S., Tielens, A. G. G. M., Ceccarelli, C., et al. 2003, ApJL, 593, L51

Curtis, E. I., Richer, J. S., Swift, J. J., & Williams, J. P. 2010, MNRAS, 408, 1516

De Simone, M., Ceccarelli, C., Codella, C., et al. 2020, ApJL, 896, L3

Dunham, M. M., Arce, H. G., Allen, L. E., et al. 2013, AJ, 145, 94

Endres, C. P., Schlemmer, S., Schilke, P., Stutzki, J., & Müller, H. S. P. 2016, Journal of Molecular Spectroscopy, 327, 95

Gerin, M., Pety, J., Commerçon, B., et al. 2017, A&A, 606, A35

Graninger, D. M., Wilkins, O. H., & Öberg, K. I. 2016, ApJ, 833, 125

Hatchell, J., Fuller, G. A., Richer, J. S., Harries, T. J., & Ladd, E. F. 2007, A&A, 468, 1009

Hatchell, J., Richer, J. S., Fuller, G. A., et al. 2005, A&A, 440, 151

Higuchi, A. E., Sakai, N., Watanabe, Y., et al. 2018, ApJS, 236, 52

Hirota, T., Bushimata, T., Choi, Y. K., et al. 2008, PASJ, 60, 37

Imai, M., Oya, Y., Sakai, N., et al. 2019, ApJL, 873, L21

Imai, M., Sakai, N., Oya, Y., et al. 2016, ApJL, 830, L37

Jorgensen, J. K., Belloche, A., & Garrod, R. T. 2020, arXiv e-prints, arXiv:2006.07071

Jørgensen, J. K., Johnstone, D., Kirk, H., et al. 2008, ApJ, 683, 822

Jørgensen, J. K., van der Wiel, M. H. D., Coutens, A., et al. 2016, A&A, 595, A117

Ko, C.-L., Liu, H. B., Lai, S.-P., et al. 2020, ApJ, 889, 172

Law, C. J., Öberg, K. I., Bergner, J. B., & Graninger, D. 2018, ApJ, 863, 88

Lee, C.-F., Li, Z.-Y., Ho, P. T. P., et al. 2017, ApJ, 843, 27

Marcelino, N., Gerin, M., Cernicharo, J., et al. 2018, A&A, 620, A80

McGuire, B. A. 2018, ApJS, 239, 17

McMullin, J. P., Waters, B., Schiebel, D., Young, W., & Golap, K. 2007, in Astronomical Society of the Pacific Conference Series, Vol. 376, Astronomical Data Analysis Software and Systems XVI, ed. R. A. Shaw, F. Hill, & D. J. Bell, 127

Möller, T., Endres, C., & Schilke, P. 2017, A&A, 598, A7

Müller, H. S. P., Schlöder, F., Stutzki, J., & Winnewisser, G. 2005, Journal of Molecular Structure, 742, 215

Müller, H. S. P., Thorwirth, S., Roth, D. A., & Winnewisser, G. 2001, A&A, 370, L49

Murillo, N. M., van Dishoeck, E. F., Tobin, J. J., & Fedele, D. 2016, A&A, 592, A56

Ortiz-León, G. N., Loinard, L., Dzib, S. A., et al. 2018, ApJ, 865, 73

Oya, Y., Sakai, N., López-Sepulcre, A., et al. 2016, ApJ, 824, 88

Oya, Y., Sakai, N., Watanabe, Y., et al. 2017, ApJ, 837, 174

Pickett, H. M., Poynter, R. L., Cohen, E. A., et al. 1998, JQSRT, 60, 883

Rabli, D., & Flower, D. R. 2010, MNRAS, 406, 95

Sahu, D., Liu, S.-Y., Su, Y.-N., et al. 2019, ApJ, 872, 196

Sakai, N., Sakai, T., Hirota, T., Burton, M., & Yamamoto, S. 2009, ApJ, 697, 769

Sakai, N., Sakai, T., Hirota, T., & Yamamoto, S. 2010, ApJ, 722, 1633

Sakai, N., & Yamamoto, S. 2013, Chemical Reviews, 113, 8981

Sakai, N., Sakai, T., Hirota, T., et al. 2014, Nature, 507, 78

Sakai, N., Oya, Y., López-Sepulcre, A., et al. 2016, ApJL, 820, L34

Schöier, F. L., van der Tak, F. F. S., van Dishoeck, E. F., & Black, J. H. 2005, A&A, 432, 369

Stephens, I. W., Dunham, M. M., Myers, P. C., et al. 2018, ApJS, 237, 22

Stephens, I. W., Bourke, T. L., Dunham, M. M., et al. 2019, ApJS, 245, 21

Tobin, J. J., Looney, L. W., Li, Z.-Y., et al. 2016, ApJ, 818, 73

Tychoniec, Ł., Tobin, J. J., Karska, A., et al. 2018, ApJS, 238, 19

Tychoniec, Ł., Manara, C. F., Rosotti, G. P., et al. 2020, arXiv e-prints, arXiv:2006.02812

Yang, Y.-L., Evans, Neal J., I., Smith, A., et al. 2020, ApJ, 891, 61

Zhang, Y., Higuchi, A. E., Sakai, N., et al. 2018, ApJ, 864, 76

Zucker, C., Speagle, J. S., Schlafly, E. F., et al. 2020, A&A, 633, A51